

# Image Formation of Multifrequency Vibro-acoustography: Theory and Computational Simulations

Glauber T. Silva

Departamento de Tecnologia da Informação  
Universidade Federal de Alagoas  
Maceió, AL, Brasil, 57072-970  
glauber@tci.ufal.br

Matthew W. Urban

Department of Physiology and  
Biomedical Engineering  
Mayo Clinic College of Medicine  
Rochester, MN, USA, 55905  
urban.matt@mayo.edu

## Abstract

*This paper presents an extension of vibro-acoustography imaging technique. The standard technique relies on the single-frequency dynamic radiation force (or stress) produced by a highly focused dual-frequency ultrasound beam. We propose a multifrequency vibro-acoustography method based on the radiation stress generated by a beam with multiple frequencies. The system point-spread function (PSF) is obtained in terms of the acoustic emission by a point-target in response to the employed radiation stress. The PSF is evaluated for an eight- and a sixteen-element sector array transducers. Three phantom images are used to show how the system transforms them into observed data. Considering only visual criteria such as contrast and resolution, simulations show the sixteen-element sector transducer renders better images.*

## 1. Introduction

Vibro-acoustography is an imaging technique that maps the acoustic response of an object to the dynamic radiation force (or stress) of ultrasound [1]. The radiation force is produced by two overlapping ultrasound beams with slightly different frequencies [2]. This difference is usually in the kilohertz range. The radiation stress oscillates at the beat frequency of the ultrasound beams. In response to the applied stress, the object vibrates emitting an acoustic field (acoustic emission). A detector can measure the acoustic emission produced by the object. As the focal point of the system scans across the object, the magnitude (or phase, in some cases) of the measured signal is used to synthesize an image of the object. Vibro-acoustography has been studied as a potential imaging technique in clinical applications

(seen in Refs. [3, 4, 5]) and nondestructive material evaluation [6].

So far, the underlying principle of vibro-acoustography is the dynamic radiation stress with a single oscillation frequency. Thus, a vibro-acoustography image of an object represents its response to the radiation stress at the specific vibration frequency. The object response to the induced vibration by the radiation stress may vary significantly as the oscillation frequency changes. This happens because the mechanical and geometrical properties of the object may lead to different vibration resonance frequencies [7]. Applying a radiation stress on an object whose vibration frequency is near the object's resonance frequency may render a higher signal-to-noise ratio (SNR) in the detected signal. Consequently, it might be possible to improve image contrast by choosing different vibration frequencies. Alizad *et al.* [8] have set forth vibro-acoustography images of *in vitro* metastatic nodules in liver tissue with different contrasts as the vibration frequency where chosen in the range of 13.3–27.6 kHz. However, the search for better vibro-acoustography images by choosing different vibration frequencies is time-consuming. An object has to be rescanned for each chosen frequency.

In this work, we propose the use of multifrequency dynamic radiation stress in vibro-acoustography systems. We present a multifrequency vibro-acoustography image formation theory, which is applied to obtain the point-spread function (PSF) of systems based on sector array transducers [9]. The stress field formation of standard vibro-acoustography has been investigated for spherical concave [10], linear array [11], and sector array transducers [12, 13]. Here, the PSF is numerically evaluated on the focal plane for an eight- and sixteen-element sector array transducers. The transducers are driven by four different ultrasound frequencies resulting five different low-frequency bands for the system PSF. The transverse resolution achieved by each transducer is about  $1.0 \text{ mm}^2$ .

Three phantom images are proposed to show how the system transforms them into observed data. From a subjective view point using perceived contrast and spatial resolution, our results show that the sixteen-element sector transducer produces better images than those by the other transducer.

## 2. Image formation theory

A linear vibro-acoustography imaging system can be characterized by its PSF, which is defined as the response of the system to a point-target. The PSF depends on the acoustic emission of the point-target, which is caused by the dynamic radiation stress. The point-target can be modelled as an small rigid sphere whose radius  $a$  is much smaller than the wavelength of the ultrasound beams that produce the radiation stress. We, therefore, need to extend the concept of the dynamic radiation stress to a multifrequency oscillatory stress exerted on an small sphere.

### 2.1. Multifrequency radiation stress

Consider a propagating medium as an infinite, homogeneous, and lossless fluid with density  $\rho_0$  and speed of sound  $c_0$ . In a lossless medium, ultrasound waves can be fully described in terms of the velocity potential  $\phi(\mathbf{r}, t)$ , where  $\mathbf{r}$  is the position vector and  $t$  is time. The particle velocity in the medium is given by  $\mathbf{v} = -\nabla\phi$ , where  $\nabla$  is the gradient operator.

The multifrequency dynamic radiation stress may be produced by  $N$  intersecting monochromatic ultrasound beams focused at the same point in space. Each ultrasound beam has angular frequency  $\omega_n$ ,  $n = 1, 2, \dots, N$ . We assume that  $\omega_m > \omega_n$ , whenever  $m > n$  ( $m, n = 1, 2, \dots, N$ ). The difference between a pair of these frequencies is denoted by  $\Delta\omega = \omega_m - \omega_n$ . Using the superposition principle, the velocity potential of the total incident ultrasound beam is

$$\phi(\mathbf{r}, t) = \sum_{n=1}^N \hat{\phi}_n(\mathbf{r}) e^{j\omega_n t}, \quad (1)$$

where  $j$  is the imaginary unit and  $\hat{\phi}_n$  is the complex amplitude function.

To simplify our theory, we assume that the resulting ultrasound beam described in Eq. (1) behaves as  $N$  collinear plane waves in the vicinity of the system focal zone. Thus, the resulting ultrasound beam behaves like an amplitude-modulated wave in time for which  $\Delta\omega_{mn}$  are the modulation frequencies. In addition, the radiation force on the point-target (sphere) located anywhere in the imaging plane lies in the direction of the ultrasound beam.

Our problem now is to obtain the dynamic radiation force exerted on an small sphere by  $N$  collinear plane

waves. Silva *et al.* [2] have calculated the dynamic radiation force on a solid sphere due to two collinear low-amplitude acoustic plane waves. Based on that result, it is possible to show that the dynamic radiation force exerted on an small sphere by the  $N$  collinear plane waves is

$$f(t) = \pi a^2 \sum_{(m \neq n)=1}^N k_m k_n \hat{y}_{\Delta\omega_{mn}} \hat{\phi}_m \hat{\phi}_n^* \exp(j\Delta\omega_{mn} t), \quad (2)$$

where  $k_m = \omega_m/c_0$  is the wavenumber of the  $m$ -wave and  $\hat{y}_{\Delta\omega_{mn}}(m, n = 1, 2, \dots, N)$  is the dynamic radiation force function. The symbol  $*$  denotes the complex conjugate. The function  $\hat{y}_{\Delta\omega_{mn}}$  can be obtained by solving the linear acoustic scattering of the plane waves  $m$  and  $n$  by the sphere.

The radiation force described in Eq. (2) defines a force-field in space. Here, the concept of radiation stress field  $\sigma(t)$  can be introduced by dividing the radiation force  $f(t)$  by the sphere projected area  $\pi a^2$ . Thus,

$$\sigma(t) = \sum_{(m \neq n)=1}^N \hat{\sigma}_{\Delta\omega_{mn}} \exp(j\Delta\omega_{mn} t), \quad (3)$$

where

$$\hat{\sigma}_{\Delta\omega_{mn}} = k_m k_n \hat{y}_{\Delta\omega_{mn}} \hat{\phi}_m \hat{\phi}_n^* \quad (4)$$

is the radiation stress amplitudes. From Eq. (3) we see that the radiation stress has at most  $N(N-1)/2$  different unique frequency components  $\Delta\omega_{mn}$ .

### 2.2. Acoustic emission

We are now interested in calculating the acoustic emission by a point-target modelled as a rigid movable sphere. Firstly, we consider the acoustic emission due to one frequency component of the radiation stress, for instance,  $n = 1$  and  $m = 2$ . The sphere vibrates around the coordinate system origin along the  $z$ -axis. Let us suppose that the sphere vibrates in linear regime (small amplitude). The sphere vibration velocity in the steady-state is given by  $\hat{v}_{21} e^{j\Delta\omega_{21} t}$ , in which  $\hat{v}_{\Delta\omega_{21}}$  is the complex velocity amplitude. The sphere radius is much smaller than the wavelength of the irradiated wave. Hence,  $\Delta k_{21} a \ll 1$ , where  $\Delta k_{21} = \Delta\omega_{21}/c_0$  is the emitted wavenumber. The amplitude of the emitted pressure by the oscillating sphere is given [14], in spherical coordinates, by

$$\hat{p}_{\Delta\omega_{21}}(r, \theta) \underset{\Delta k_{21} a \ll 1}{\sim} \rho_0 c_0 \hat{v}_{\Delta\omega_{21}} (\Delta k_{21} a)^3 \cos \theta \frac{e^{-j\Delta k_{21} r}}{2\Delta k_{21} r}, \quad (5)$$

where ' $\sim$ ' denotes approximation. Note that this pressure field is a dipole radiation, which depend solely on the distance  $r$  and the polar angle  $\theta$ .

The velocity amplitude  $\hat{v}_{\Delta\omega_{21}}$  of sphere at frequency  $\Delta\omega_{21}$  can be described by the sphere mechanical impedance

$\hat{z}_{\Delta\omega_{21}}$  as  $\hat{v}_{\Delta\omega_{21}} = \pi a^2 \hat{\sigma}_{\Delta\omega_{21}} / \hat{z}_{\Delta\omega_{21}}$ . The acoustic outflow  $\hat{q}_{\Delta\omega_{21}}$  (the volume of the medium which is displaced per unit time due to an object vibration per unit force) by the sphere at the frequency  $\Delta\omega_{21}$  is related to the mechanical impedance by  $\hat{q}_{\Delta\omega_{21}} = 2\pi a^2 / \hat{z}_{\Delta\omega_{21}}$ . Thus, Eq. (5) may be rewritten as

$$\hat{p}_{\Delta\omega_{21}} = \rho_0 c_0 \hat{\sigma}_{\Delta\omega_{21}} \hat{q}_{\Delta\omega_{21}} \hat{g}_{\Delta\omega_{21}}, \quad (6)$$

where

$$\hat{g}_{\Delta\omega_{21}} = (\Delta k_{21} a)^3 \cos \theta \frac{e^{-j\Delta k_{21} r}}{\Delta k_{21} r}$$

is the object-medium transfer function which depends on the medium boundary-conditions and object geometry.

Now, we can generalize the acoustic emission due to a single-frequency radiation stress to that one of a multifrequency stress. For the linear vibration regime, the acoustic emission has the same frequency components as the radiation stress. By using the superposition principle, we may obtain the acoustic emission due to the radiation stress in Eq. (3) as follows:

$$p(r, \theta; t) = \sum_{(m \neq n)=1}^N \hat{p}_{\Delta\omega_{mn}}(r, \theta) e^{j\Delta\omega_{mn} t}, \quad (7)$$

where the emission amplitudes  $\hat{p}_{\Delta\omega_{mn}}$  are given by Eq. (6) changing the indices 21 by  $mn$ .

By using Eq. (4) and (6), we may write the acoustic emission amplitudes of an sphere located at the position  $\mathbf{r}$  and measured at  $\mathbf{r}'$  as follows

$$\hat{p}_{\Delta\omega_{mn}}(\mathbf{r}'|\mathbf{r}) = \rho_0 c_0 k_m k_n \hat{g}_{\Delta\omega_{mn}} \hat{q}_{\Delta\omega_{mn}} \hat{\phi}_m^* \hat{\phi}_n^* \hat{g}_{\Delta\omega_{mn}}(\mathbf{r}'|\mathbf{r}), \quad (8)$$

where

$$\hat{g}_{\Delta\omega_{mn}}(\mathbf{r}'|\mathbf{r}) = (\Delta k_{mn} a)^3 \cos \theta \frac{\exp(-j\Delta k_{mn} |\mathbf{r}' - \mathbf{r}|)}{\Delta k_{mn} |\mathbf{r}' - \mathbf{r}|}.$$

### 2.3. Point-spread function

The region of interest has to be scanned by the ultrasound beam in order to form a vibro-acoustography image. The scanning process can be accomplished by either mechanically moving the ultrasound transducer or electronically steering the beam using linear arrays. In vibro-acoustography, the image synthesis depends on the acoustic emission by the objects in the region.

In multifrequency vibro-acoustography, each frequency component  $\Delta\omega_{mn}$  of the acoustic emission may be used to generate an image of an object. Therefore, this technique produces a multiband image. The number of bands of an image is at most  $N(N-1)/2$ , which is the number of frequency components  $\Delta\omega_{mn}$ .

To define the image of an object we need to represent it through a function. Referring to Eq. (8), the terms that depend on the object are the dynamic radiation force function

$\hat{y}_{\Delta\omega_{mn}}$  and the acoustic outflow  $\hat{q}_{\Delta\omega_{mn}}$  at the frequency  $\Delta\omega_{mn}$ . We assume that the acoustic emission of an object (or region) is a linear combination of the emission of every infinitesimal volume in the object. For an infinitesimal volume, the acoustic emission at the frequency  $\Delta\omega_{mn}$  is given by Eq. (8). The functions  $\hat{y}_{\Delta\omega_{mn}}$  and  $\hat{q}_{\Delta\omega_{mn}}$  may vary within the object. Thus, we define the object function as

$$\hat{o}_{\Delta\omega_{mn}}(\mathbf{r}) = \hat{y}_{\Delta\omega_{mn}}(\mathbf{r}) \hat{q}_{\Delta\omega_{mn}}(\mathbf{r}), \quad m \neq n.$$

The  $\Delta\omega_{mn}$ -band of the image of an object is, thus, given by

$$\hat{i}_{\Delta\omega_{mn}}(\mathbf{r}) = \hat{o}_{\Delta\omega_{mn}}(\mathbf{r}) \star \hat{h}_{\Delta\omega_{mn}}(\mathbf{r}), \quad (9)$$

where  $\hat{h}_{\Delta\omega_{mn}}(\mathbf{r})$  is the  $\Delta\omega_{mn}$ -band PSF of the system and the symbol  $\star$  denotes spatial convolution. Note the image function  $\hat{i}_{\Delta\omega_{mn}}(\mathbf{r})$  is complex.

In analogy with the definition of the single-frequency vibro-acoustography PSF [15], we may define the  $\Delta\omega_{mn}$ -band PSF in terms of the ultrasound fields as

$$\hat{h}_{\Delta\omega_{mn}}(\mathbf{r}) \equiv A \hat{\phi}_m(\mathbf{r}) \hat{\phi}_n^*(\mathbf{r}), \quad (10)$$

where  $A$  is a normalization constant.

The spatial resolution of an imaging system is proportional to the width of the mainlobe of the PSF [16]. Hence, we define the spatial resolution cell of the vibro-acoustography system as the volume enclosed by the mainlobe of the PSF at  $-12$  dB.

### 2.4. Stress field forming

Here, we consider an eight- and a sixteen-element sector array transducers with aperture radius  $a$  and focal distance  $z_0$  (see Fig. 1 for geometric description). Each array element is driven by a sinusoidal signal. The signals of the first four elements have frequencies in the following sequence  $\omega_1, \omega_2, \omega_3$ , and  $\omega_4$ , counterclockwise. This sequence is repeated for the rest of array elements in the same order. Hence, the transducers operated at four different frequencies yielding an image with at most six unique bands.

Let  $\hat{\phi}_m$  ( $m = 1, 2, 3, 4$ ) be the velocity potential amplitude generated by a pair of symmetric elements of the sector transducer. The  $\Delta\omega_{mn}$ -band PSF on the focal plane is given by

$$\hat{h}_{\Delta\omega_{mn}}(r, \theta) = A \hat{\phi}_m(r, \theta) \hat{\phi}_n^*(r, \theta), \quad m(\neq n) = 1, 2, 3, 4. \quad (11)$$

Notice that  $r$  and  $\theta$  are polar variables in the focal plane. The velocity potential  $\hat{\phi}_m$  is given by Eq. (12) in which  $J_\ell$  is the  $\ell$ th-order Bessel function of first-kind and  $\bar{k}_m = 2k_m/F$  with  $k_m = \omega_m/c_0$ . The quantity  $F = z_0/(2a)$  is the transducer  $F$ -number. The amplitude function  $\hat{a}_m$  is given by

$$\hat{a}_m = 2av_0 \exp \left[ -jk_m \left( z_0 + \frac{r^2}{2z_0} \right) \right], \quad (13)$$

$$\hat{\phi}_m(r, \theta) = \frac{\hat{a}_m}{\bar{k}_m r} \sum_{\ell=0}^{+\infty} \left[ \varrho_{(2\ell)m}(\theta) J_{2\ell+1}(\bar{k}_m r) + \frac{4(\ell+1)}{\bar{k}_m r} \sum_{\ell'=0}^{+\infty} J_{2(\ell+\ell'+2)}(\bar{k}_m r) \right]. \quad (12)$$

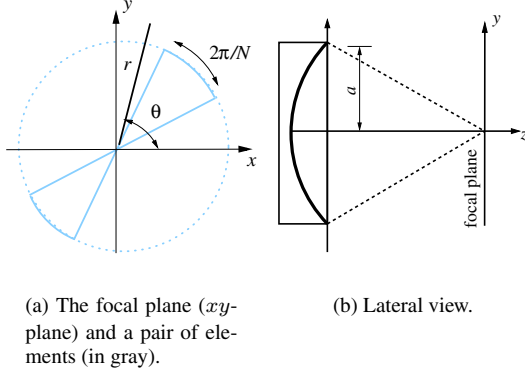


Figure 1: Geometric description of the sector array transducer and the focal plane.

where  $v_0$  is the normal velocity amplitude on the transducer element. The angular function  $\varrho_{\ell m}$  is

$$\varrho_{\ell m}(\theta) = \frac{(-1)^\ell}{\ell} \cos \left[ \ell \left( \theta - \frac{2m+1}{4} \pi \right) \right] \sin \left( \frac{\ell \pi}{8} \right), \quad (14)$$

where  $\ell = 1, 2, \dots$  and  $\varrho_{0m} = \pi/4$ .

The leading term of Eq. (12) is  $\pi J_1(\bar{k}_m r)/(4\bar{k}_m r)$ , which corresponds to the radiation produced by an spherical concave transducer. Further, the velocity potential is circularly symmetric.

### 3. Computational simulation

#### 3.1. Numerical evaluation

We evaluated the PSF of sector array transducers with eight and sixteen elements with similar characteristics to those found in commercial transducers. The aperture size and focal distance are, respectively, 47 mm and  $z_0 = 75$  mm. Each pair of opposite symmetric elements is driven by a sinusoidal signal. The driving frequencies are 2.00, 2.03, 2.04, and 2.05 MHz. Thus, the imaging system produces five different bands, namely,  $\Delta f_{21} = 30$  kHz,  $\Delta f_{31} = 40$  kHz,  $\Delta f_{41} = 50$  kHz,  $\Delta f_{32} = \Delta f_{43} = 10$  kHz, and  $\Delta f_{42} = 20$  kHz. Because the 10 kHz band appears twice, the maximal magnitude of the radiation stress of this band is twice that of the other bands. The speed of sound in the water is assumed to be  $c_0 = 1500$  m/s.

Magnitude images have been mostly used in vibro-acoustography medical imaging applications [5]. Phase images seem to have less contrast details compared to magnitude ones. Thus, hereafter the system PSF will be referred to the magnitude of the function  $\hat{h}_{\Delta\omega_{mn}}$ . The PSFs were evaluated here through Eq. (10) combined with Eq. (12).

In Fig. 2, we have the five bands of the PSF for the eight-element sector transducer with the corresponding active array elements. The transverse resolution of each band is about  $1.0 \text{ mm}^2$ . Sidelobe levels for all PSF bands are below  $-7$  dB. The 20 and 40 kHz bands are equivalent, differing only in the spatial orientation of their lobes; the same happens with the 30 and 50 kHz bands.

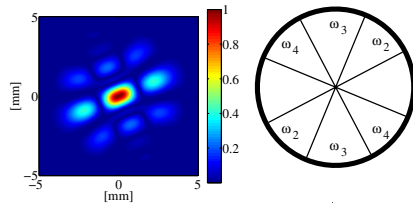
The PSF bands of the sixteen-element sector transducer with their respective active array elements are shown in Fig. 3. The spatial resolution of the bands are about the same as its eight-element counterpart. Sidelobe levels are under  $-8.5$  dB for the 20 and 40 kHz bands, while for the 10, 30 and 50 kHz bands we have  $-13$  dB. The 20 and 40 kHz bands are equivalent as well as the 30 and 50 kHz bands.

#### 3.2. Image phantoms

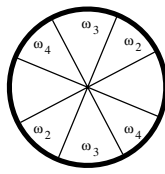
To evaluate how the PSF distorts objects, we designed the three phantoms shown in Fig. 4. The phantoms in Figs. 4(a) and 4(b), namely Phantom-1 and Phantom-2, are composed of lines equally spaced at, respectively, 0.6 mm and 1.2 mm. The objects in Fig. 4(c) were chosen to mimic tissue mass lesions (circles) and brachytherapy metal seeds (rectangles) with varying orientation and contrast. The imaging process of the phantoms is carried out through the convolution of the object function with the PSF bands as described in Eq. (9). To image Phantom-1 and Phantom-2 we used only the 10, 20, and 50 kHz PSF bands because they are intrinsically different to each other. Phantom-3 was imaged only by the 10 and 50 kHz PSF bands because they have lower sidelobes.

Figure 5 shows images of Phantom-1 and -2 produced by the eight-element sector transducer. The 10 and 50 kHz PSF bands did not resolve, respectively, vertical and horizontal lines present in Phantom-1. Images of Phantom-2 are distorted exhibiting different patterns.

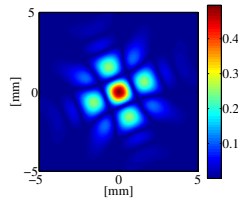
Figure 6 presents images of Phantom-1 and Phantom-2 generated by the sixteen-element sector transducer. Images of Phantom-1 exhibit a fairly good resolution, with the exception of the one pro-



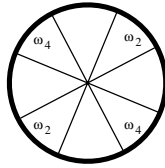
(a) 10 kHz



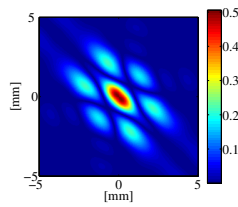
(b)



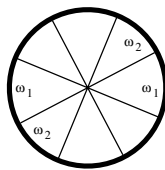
(c) 20 kHz



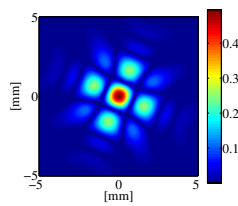
(d)



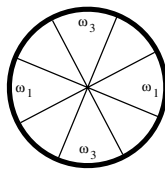
(e) 30 kHz



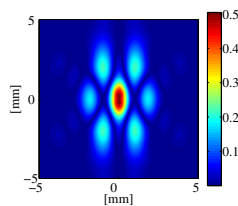
(f)



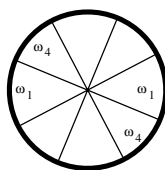
(g) 40 kHz



(h)

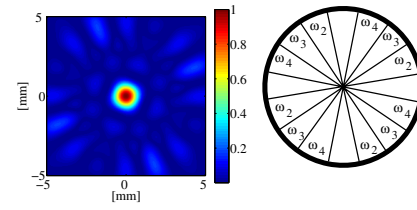


(i) 50 kHz

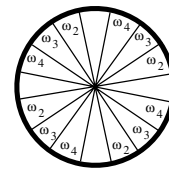


(j)

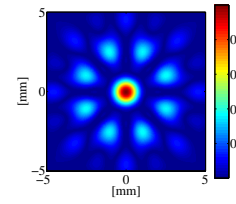
Figure 2: The PSFs of the eight-element sector transducer.



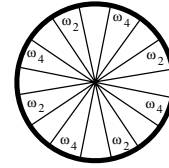
(a) 10 kHz



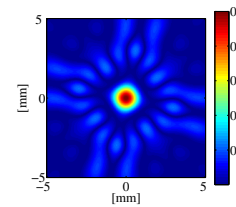
(b)



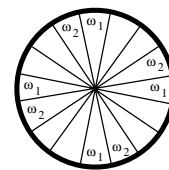
(c) 20 kHz



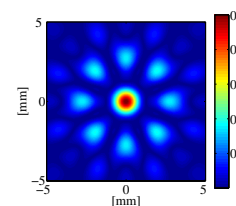
(d)



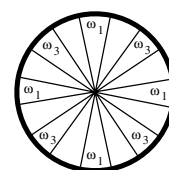
(e) 30 kHz



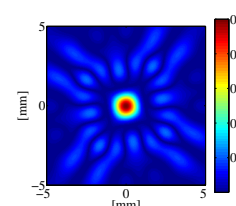
(f)



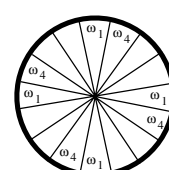
(g) 40 kHz



(h)

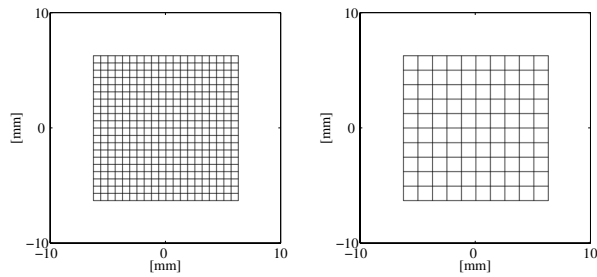


(i) 50 kHz



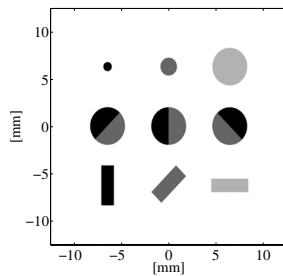
(j)

Figure 3: The PSFs of the sixteen-element sector transducer.



(a) Phantom-1: line spacing 0.6 mm.

(b) Phantom-2: line spacing 1.2 mm.



(c) Phantom-3.

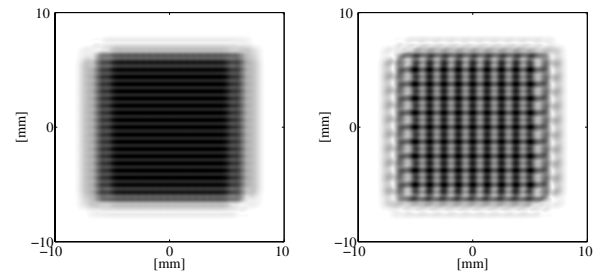
Figure 4: Three phantoms for vibro-acoustography.

duced by the 20 kHz band. The resolution and contrast of Phantom-2 images are good. These images are slightly distorted on the edges of the phantom.

Images of Phantom-3 are shown in Fig. 7. The images made by the eight-element sector transducer present relatively poor contrast for the center and the rightmost brachytherapy seeds and the top rightmost mass lesion. Further, the contrast inside the centered mass lesions in the 50 kHz image band is blurred due to the high level side-lobes. The sixteen-element sector transducer rendered better images. All structures can be seen in the 10 kHz image band with good contrast quality. The 50 kHz image band shows the objects a little bit distorted.

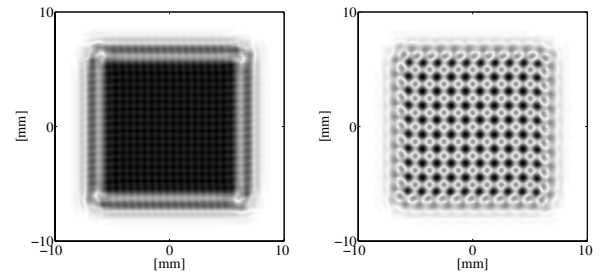
#### 4. Discussion and conclusion

We have presented an image formation theory for multifrequency vibro-acoustography. The multiband PSF was computed from the acoustic emission of a point-target induced by multifrequency radiation stress in a lossless fluid. This stress may be different depending on the medium attenuation properties. A theory for the dynamic acoustic radiation force in attenuating media has not yet been developed in the literature.



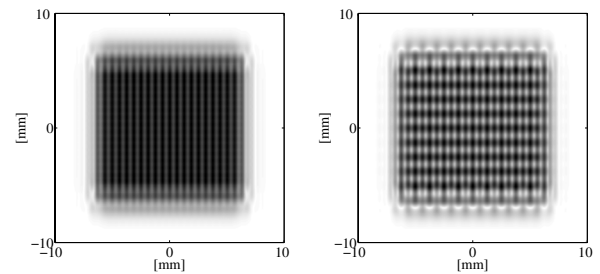
(a) Phantom-1 at 10 kHz.

(b) Phantom-2 at 10 kHz.



(c) Phantom-1 at 20 kHz.

(d) Phantom-2 at 20 kHz.



(e) Phantom-1 at 50 kHz.

(f) Phantom-2 at 50 kHz.

Figure 5: Magnitude images by the eight-element transducer.

Sector array transducers with eight and sixteen elements were modelled to produce multiband vibro-acoustography images. Such transducers are commercially available and, thus, suitable for preliminary multifrequency vibro-acoustography studies. Both transducers were driven by four sinusoidal signals different frequencies which are around 2 MHz. The transverse resolution produced by both transducers is around  $2.0 \text{ mm}^2$ . Such resolution can be further improved by increasing the driving frequencies or augmenting the aperture size.

Images of Phantom-1 by both transducers are blurred

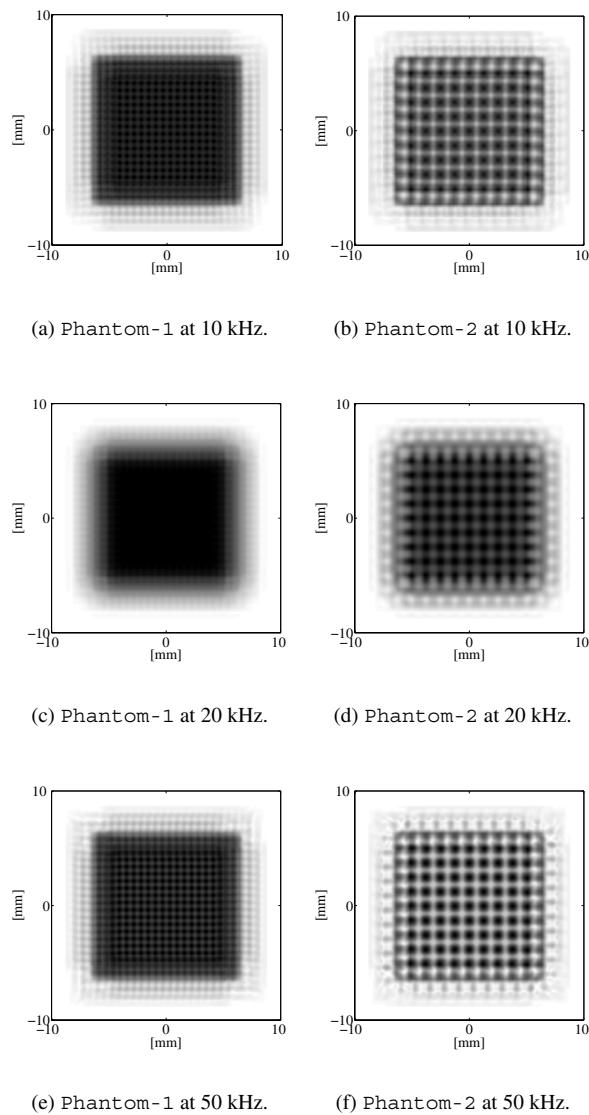


Figure 6: Magnitude images by the sixteen-element transducer.

because the line spacing is about half of the system lateral resolution. Phantom-2 was fairly resolved by the transducers; however, different artifacts appeared took place in each image band. This happened, mainly, because high sidelobes with different spatial orientation are present in the PSF bands (see Figs. 2 and 3). Sidelobes produced by the sixteen-element sector transducer ( $-13$  dB) are almost two times as small as those produced by the eight-element transducer. The sidelobe levels are still too high compared to those produced by spherical two-element confocal transducers ( $-34$  dB) [13], which are widely used in vibro-

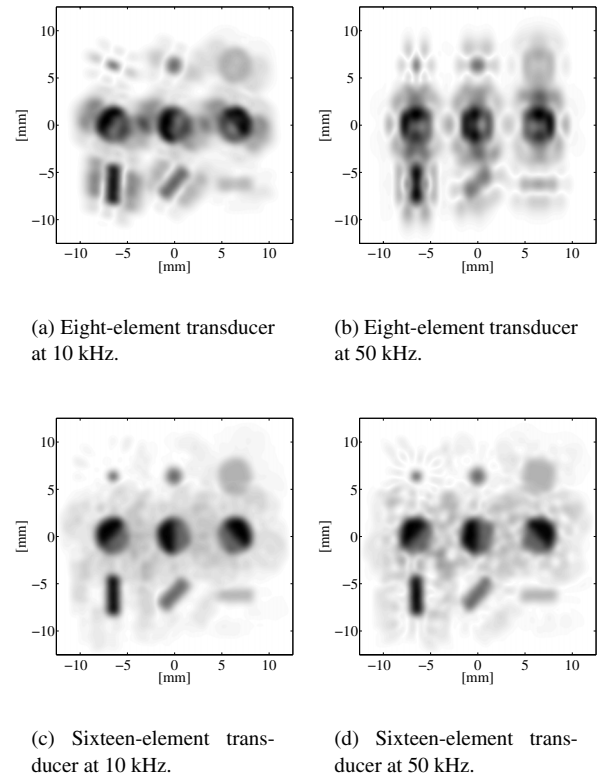


Figure 7: Magnitude images of Phantom-3.

acoustography *in vitro* applications.

Improvement on sidelobes produced by multifrequency vibro-acoustography systems based on sector array transducers needs further investigation. Mismatching the ultrasound beams that produce the radiation stress field may reduce sidelobes. Moreover, using a sector transducer with thirty-two elements and keeping four different driving frequencies may yield lower sidelobes. An alternative for sector transducers in multifrequency vibro-acoustography applications are linear arrays. These transducers allow beam steering and focusing by electronically de-phasing the driving signals applied to the array elements. Linear arrays were already studied for vibro-acoustography systems [11].

Images of Phantom-3 revealed how the imaging system distorted objects. High sidelobes degraded the contrast in the images. However, the 10 kHz band produced by the sixteen-element sector transducer exhibited reasonable contrast and resolution. The depth-of-field of the system PSF was not taken into account on the image simulations.

In multifrequency vibro-acoustography, we gain information at many more vibration frequencies within the time it takes to do one scan. As presented in the paper, we have five-fold more information in the acquired data from the

acoustic emission than for the single frequency case. This information gain is at the expense of reducing the amount of acoustic emission received in comparison to the similar single frequency scanning. Thus, this may reduce the signal-to-noise ratio in some image bands.

The contrast of vibro-acoustography images may vary with object resonance frequencies. Including object resonances in the vibro-acoustography image formation theory is out of the scope of this paper.

In conclusion, a vibro-acoustography technique that produces multiband images was proposed. Simulated images presented are encouraging for future experimental system development.

## Acknowledgments

The authors would like to thank **Dr. Alejandro Frery** for helpful discussions. This work was partially supported by grant DCR013.2003-FAPEAL/CNPq (Brazil).

## References

- [1] M. Fatemi and J. F. Greenleaf, "Ultrasound-stimulated vibro-acoustic spectrography," *Science*, vol. 280, pp. 82–85, 1998.
- [2] G. T. Silva, S. Chen, J. F. Greenleaf, and M. Fatemi, "Dynamic ultrasound radiation force in fluids," *Physical Review E*, vol. 17, p. 056617, May 2005.
- [3] A. Alizad, M. Fatemi, R. A. Nishimura, R. R. Kinnick, E. Rambod, and J. F. Greenleaf, "Detection of calcium deposits on heart valve leaflets by vibro-acoustography: an in vitro study," *Journal of the American Society of Echocardiography*, vol. 15, no. 11, pp. 1391–1395, November 2002.
- [4] F. G. Mitri, P. Trompette, and J. Chapelon, "Improving the use of vibro-acoustography for brachytherapy metal seed imaging: a feasibility study," *IEEE Transactions on Medical Imaging*, vol. 23, no. 1, pp. 1–6, January 2004.
- [5] A. Alizad, M. Fatemi, L. E. Wold, and J. F. Greenleaf, "Performance of vibro-acoustography in detecting microcalcifications in excised human breast tissue: a study on 74 tissue samples," *IEEE Transactions on Medical Imaging*, vol. 23, no. 3, pp. 307–312, 2004.
- [6] M. Fatemi, J. F. Greenleaf, and A. Manduca, "Imaging elastic properties of biological tissues by low-frequency harmonic vibration," *Proceedings in the Institute of Electric and Electronics Engineers*, vol. 91, pp. 1503–1519, October 2003.
- [7] F. G. Mitri, Z. E. A. Fellah, E. Closset, P. Trompette, and J. Chapelon, "Determination of object resonances by vibro-acoustography and their associated modes," *Ultrasonics*, vol. 42, pp. 537–543, 2004.
- [8] A. Alizad, L. E. Wold, J. F. Greenleaf, and M. Fatemi, "Imaging mass lesions by vibro-acoustography: modeling and experiments," *IEEE Transactions on Medical Imaging*, vol. 23, no. 9, pp. 1087–1093, 2004.
- [9] C. A. Cain and S. Umemura, "Concentric-ring and sector-vortex phased-array applicators for ultrasound hyperthermia," *IEEE Transactions on Microwave Theory and Techniques*, vol. MTT-34, no. 5, pp. 542–551, May 1986.
- [10] S. Chen, M. Fatemi, R. Kinnick, and J. F. Greenleaf, "Comparison of stress field forming methods for vibro-acoustography," *IEEE Transactions on Ultrasonics, Ferroelectrics, and Frequency Control*, vol. 51, no. 3, pp. 313–321, March 2004.
- [11] G. T. Silva, J. F. Greenleaf, and M. Fatemi, "Linear arrays for vibro-acoustography: a numerical simulation study," *Ultrasonic Imaging*, vol. 26, pp. 1–17, April 2004.
- [12] G. T. Silva, S. Chen, E. Almeida, A. Frery, M. Fatemi, and J. F. Greenleaf, "Image formation in vibro-acoustography with sector array transducers," in *XVII SIBGRAP*. Computer, 2004, pp. 25–32.
- [13] G. T. Silva, S. Chen, A. Frery, J. F. Greenleaf, and M. Fatemi, "Stress field forming of sector array transducers for vibro-acoustography," Accepted for publication in *IEEE Transactions on Ultrasonics, Ferroelectric, and Frequency Control*, March 2005.
- [14] P. R. Wallace, *Mathematical Analysis of Physical Problems*. New York: Dover, 1984, p. 239.
- [15] M. Fatemi and J. F. Greenleaf, "Vibro-acoustography: an imaging modality based on ultrasound-stimulated acoustic emission," *Proceedings of the National Academy of Sciences of the United States of America*, vol. 96, pp. 6603–6608, June 1999.
- [16] G. Wang and Y. Li, "Axiomatic approach for quantification of image resolution," *IEEE Signal Processing Letters*, vol. 6, no. 10, pp. 257–258, 1999.